2022

Emissivity prediction of functionalized surfaces using artificial intelligence

Greg Acosta

Andrew Reicks

Miguel Moreno

Alireza Borjali

Craig Zuhlke

See next page for additional authors

Authors
Greg Acosta, Andrew Reicks, Miguel Moreno, Alireza Borjali, Craig Zuhlke, and Mohammad Ghashami

Emissivity prediction of functionalized surfaces using artificial intelligence

Greg Acosta,[1] Andrew Reicks,[2] Miguel Moreno,[1]
Alireza Borjali,[3,4] Craig Zuhlke,[2]
& Mohammad Ghashami [1]

1 Mechanical & Materials Engineering Department,
University of Nebraska–Lincoln, Lincoln, NE, 68588, USA

2 Electrical & Computer Engineering Department,
University of Nebraska–Lincoln, Lincoln, NE 68588, USA

3 Harris Orthopaedics Laboratory, Department of
Orthopaedic Surgery, Massachusetts General Hospital,
Boston, MA 02114, USA

4 Department of Orthopaedic Surgery,
Harvard Medical School, Boston, MA 02115, USA

Corresponding author — M. Ghashami, *email* mghashami2@unl.edu

Abstract

Tuning surface emissivity has been of great interest in thermal radiation applications, such as thermophotovoltaics and passive radiative cooling. As a low-cost and scalable technique for manufacturing surfaces with desired emissivities, femtosecond laser surface processing (FLSP) has recently drawn enormous attention. Despite the versatility offered by FLSP, there is a knowledge gap in accurately predicting the outcome emissivity prior to fabrication. In this work, we demonstrate the immense advantage of employing artificial intelligence (AI) techniques to predict the emissivity of complex surfaces. For this aim, we used FLSP to fabricate 116 different aluminum samples. A comprehensive dataset

Published in *Journal of Quantitative Spectroscopy & Radiative Transfer* 291 (2022) 108325
doi:10.1016/j.jqsrt.2022.108325

Submitted 14 January 2022; revised 8 July 2022; accepted 17 July 2022; published 20 July 2022.

was established by collecting surface characteristics, laser operating parameters, and the measured emissivities for all samples. We demonstrate the successful application of AI in two distinct scenarios: (1) effective emissivity classification solely based on 3D surface morphology images, and (2) emissivity prediction based on surface characteristics and FLSP parameters. These findings open new pathways towards extended implementation of AI to predict various surface properties in functionalized samples or extract the required fabrication parameters via reverse engineering.

Keywords: Emissivity, Functionalized surfaces, Artificial intelligence, Thermal radiation, Femtosecond laser surface processing

1. Introduction

Altering the emissivity of real surfaces is of great interest in many engineering applications, such as thermal protection systems for aerospace vehicles [1–3], passive radiative cooling [4, 5], thermophotovoltaics (TPVs) [6, 7], and thermal management systems [8 , 9]. Several methods have been suggested in the literature to modify a surface's radiative response, including applying coatings and paints on the surface, fabricating metamaterials, or functionalizing surfaces.

Coatings and paints can modify the electrical and optical properties of a material by introducing impurities in the form of nanocomposites, metallic powders, or polymers to a surface [10]. Their ease of implementation on large or curved surfaces has given rise to their applications in TPV emitters [11], radiation pyrometry [12 , 13], heating and cooling [14 , 15], and thermal imaging [16 , 17]. However, being susceptible to lamination and wear due to variations in environmental conditions limits their applications. In a different approach, the fabrication of metamaterials has been pursued to obtain surfaces with desired spectral and directional emissivity [18–20]. Metamaterials can exhibit wavelength-selective properties by carefully fabricating subwavelength nanostructures on the surface that can enhance [21] or lower [22] the emissive power. However, their tailored response is often limited to a narrow spectral band and requires costly microfabrication processes. An alternative way to tune the emissivity of larger surfaces can be achieved via surface functionalization, which is a process that involves the combination of physical (e.g., texturing/patterning) and chemical modification of surfaces [23]. One way to produce functionalized surfaces is by

using femtosecond laser surface processing (FLSP), a unique process to directly modify the surface morphology of almost any material, thus altering their broadband absorption or emission response [24–26]. In addition to their simple fabrication process, FLSP surfaces show remarkably wider bandwidth response, and great permanency and durability even in extreme environments [27].

Despite the tremendous technological advancements in fabrication processes of engineered surfaces, there still remains a significant challenge in accurately predicting the outcome of these processes. An accurate prediction of the emissivity from the envisioned engineered surfaces can significantly cut the time and labor cost of the required fabrication processes. In principle, this would be feasible by understanding how various surface patterns and microstructures affect the interaction of electromagnetic waves with the surface. However, trying to correlate the geometrical attributes of the quasiperiodic surface structures to the measured emissivity via physics-based or model-driven approaches can be a cumbersome task due to the multifaceted nature of the problem. In such complex problems, artificial intelligence (AI) techniques can be employed to act as facilitators to find the linkage between the inputs (e.g., laser parameters and surface characteristics) and the outputs (i.e., emissivity).

Recently, AI-based data-driven models of physical processes in various fields have demonstrated great potential to accurately predict physical properties [28–31]. For example, Kang *et al.* [32] used machine-learning methods to predict radiative properties of dispersed media as a function of packed bed geometry and material properties. In another study, Mishra *et al.* [33] implemented a special data-driven algorithm based on physics-informed neural networks (PINNs) [34] to simulate radiative transfer. Their model demonstrated remarkable performance in accurately finding an unknown absorption coefficient from measurements of incident radiation. Borjali *et al.* [35] developed a data-driven model for predicting the wear rate of orthopedic polyethylene as a function of the wear experiment's parameters such as velocity and contact area. In a different application, Xiong *et al.* [36] developed an AI predictive model to understand the effect of alloy composition on the shear and bulk modulus of new bulk metallic glasses (BMGs). In an effort to predict the surface roughness of additively manufactured Ti-6Al-4V, Akhil *et al.* [37] developed a predictive model by using AI to extract texture parameters from scanning electron microscopy (SEM) images.

Besides the massive advantage in developing predictive data-driven models, AI techniques can also be implemented for inverse design and optimization problems. For instance, in nanophotonics, AI is used to optimize photonic structures' subwavelength geometrical features and their optical response [38]. Peurifoy *et al.* [39] used deep neural networks (DNNs) first to predict the light scattering of a multilayered core-shell nanoparticle. Once trained, the DNN was used to optimize the total number of layers and their thicknesses required to achieve a desired optical response. Similarly, So *et al.* [40] used a special DNN architecture to simultaneously design and output the optimal material and layer thickness of spherical three-layered nanoparticles based on a set of desired electric and magnetic dipole resonances as the input. In another application, Liu *et al.* [41] implemented an ensemble of convolutional neural networks (CNNs) to generate optimal surface patterns for structured metasurfaces, where the input to the network was a desired spectral transmittance distribution. Lastly, Garcia *et al.* [42] demonstrated how deep-learning techniques could be implemented for the modeling and inverse design of radiative heat transfer phenomena in various systems, including hyperbolic metamaterials, passive radiative cooling in photonic-crystals, and emissive power of subwavelength objects.

The aforementioned studies are just a handful of many diverse research projects where the applications of AI have proven to be of significant importance in the analysis of data, prediction of physical properties, and inverse design of physical phenomena. In this study, we demonstrate how AI techniques can be employed to successfully predict the hemispherical emissivity of aluminum surfaces processed by FLSP. In the following sections, the sample fabrication, preparation, and characterization processes will be discussed in detail, followed by the AI implementation process and a discussion of the results.

2. Sample Preparation and Fabrication via FLSP

In this work, we employed FLSP manufacturing technique to directly modify the surface properties of bulk aluminum alloy 6061 samples in a well-controlled manner. FLSP can form quasi-periodic patterns of self-organized microstructures. The geometrical structure of these permanent surface features mostly resembles micro-/nano-scale mounds or

pyramids, coated by a thin layer of redeposited nanoparticles [27]. The surface chemistry and subsurface microstructure will also be altered by FLSP, leading to very unique surface properties for each sample [43]. By adjusting the processing parameters of FLSP, such as laser fluence (i.e., energy per surface area), laser pulse count, and the atmospheric environment, one can directly control the resultant surface morphology and chemistry [44].

FLSP has many advantages over other surface functionalization methods: it results in a fully functionalized surface in a single processing step; it is a scalable process; it involves the creation of hierarchical micro-/nano-scale surface features composed of the original material, making the surface highly permanent; it modifies the original surface without the net addition of mass; and, it results in a small heat affected zone, so the surface can be modified without altering the bulk properties of the materials [45]. More importantly, FLSP surfaces can produce omnidirectional emissivity due to high absorption at large incident angles, which is very difficult to achieve via coatings, paints, or metamaterials [27 , 46].

Prior to performing FLSP, the samples were cleaned by wetting with ethanol and let dry to remove any contamination. Afterward, the samples were placed on a motorized stage within an open-air environment, where the surface processing occurs. A typical setup to apply FLSP is shown in **Fig. 1**, consisting of a femtosecond laser system, beam delivery and focusing optics, and a motorized 3D stage where the samples are placed. The laser used was a Coherent Inc. Astrella Ti:sapphire laser system that produces 6 mJ, 35 fs pulses at a 1 kHz repetition rate, with a central wavelength of 800 nm. The pulses were focused onto the sample surface using a 150 nm focal length plano-convex lens. The laser output is quantified via two laser processing parameters: fluence (F_p) and pulse count (P_c). The fluence values given are the peak fluence, which is the fluence at the peak of the Gaussian distribution of the focused pulses. Fluence is the energy per unit area (J/cm^2), and is defined as,

$$F_p = \frac{2P}{\pi\omega^2 R} \tag{1}$$

where P is the average power, ω is the $1/e^2$ beam radius, and R is the repetition rate of the laser. In order to process an area larger than that of the beam, a raster scanning pattern is utilized. The laser is used to scan

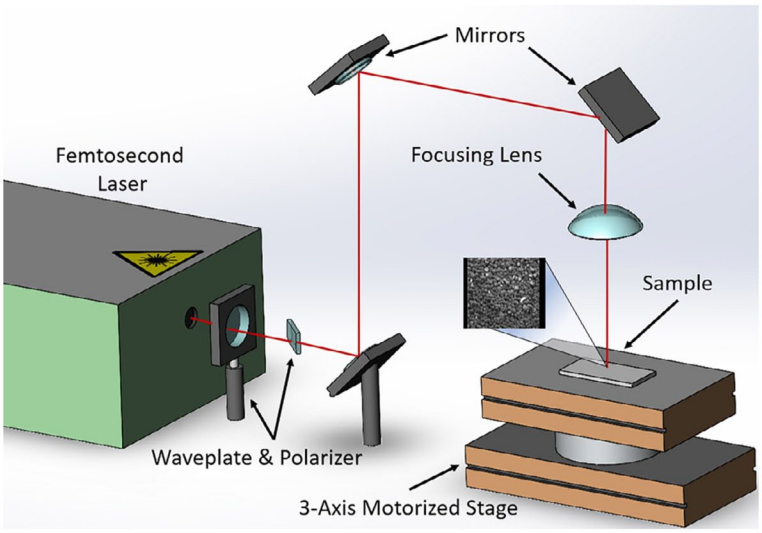

Fig. 1. Schematic illustration of the femtosecond laser surface processing setup. The samples are mounted on 3-axis motorized stages that control the processing pattern of the laser. Since the beam diameter is small compared to the size of the processed area, a rastering pattern is used to effectively cover the surface.

a line in the x–direction, and then the motorized stage is stepped over in the y–direction. The step distance between line scans is referred to as the pitch, p. The pulse count considers the overlap in the pitch and scan directions to calculate the number of pulses incident at each point on the surface and is defined as,

$$P_c = \frac{\pi R \omega^2}{vp} \tag{2}$$

where v is the stage velocity. Optimizing the fluence and pulse count is a crucial step in fabricating a desired surface as they dictate the shape and periodicity of the microstructures and the thickness of the oxide layer forming on the surface.

In order to produce the 116 aluminum samples used for this study, the fluence was varied between 0.06 and 5.5 (J/cm^2) and the pulse counts between 270 and 140 0 0. **Fig. 2** shows surface SEM images of four of the aluminum samples after the FLSP is performed. From Fig. 2, the formation of quasiperiodic self-organized microstructures can be observed. Note the different morphology of the micro-/nano-scale surface features that develop via FLSP for different fluence and pulse count values.

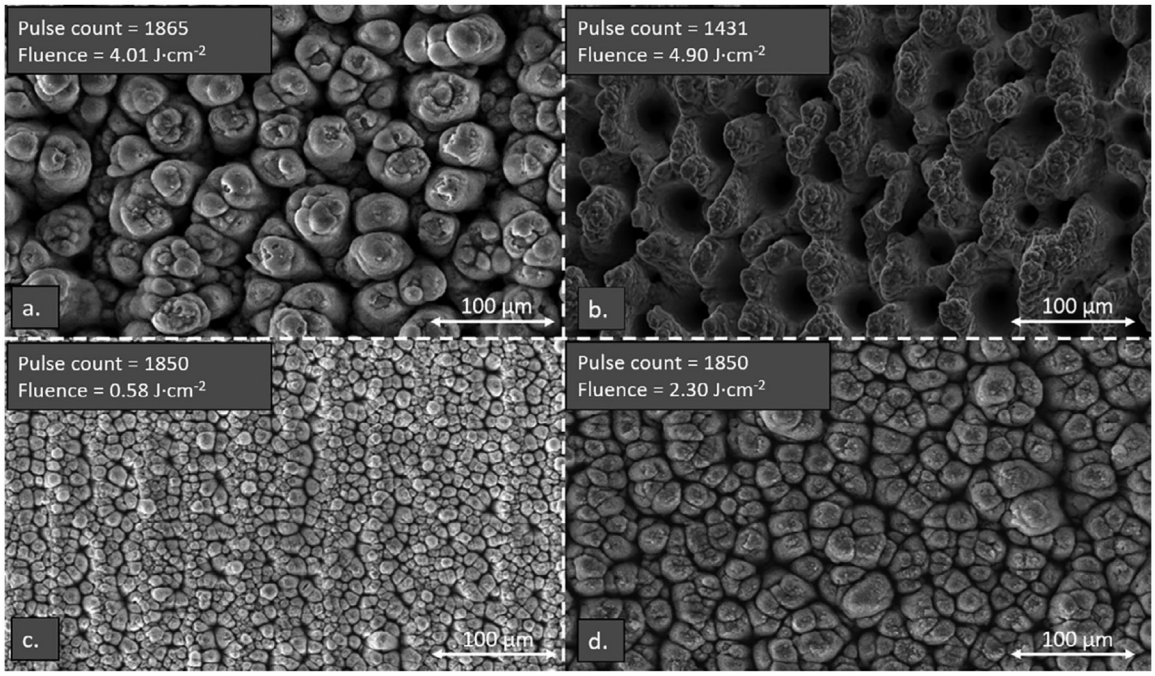

Fig. 2. Surface SEM images of the aluminum samples with quasi-periodic microstructures produced by FLSP. The laser parameters of pulse count and fluence are shown on each image. The resultant measured hemispherical emissivities are (a) $\varepsilon_h = 0.926$, (b) $\varepsilon_h = 0\,.\,865$, (c) $\varepsilon_h = 0\,.\,781$, and (d) $\varepsilon_h = 0\,.\,926$.

3. Surface characterization and emissivity measurement

In order to fully characterize the surface features of the FLSP samples, laser scanning confocal microscopy (LSCM, Keyence VK-X200K) with 500 nanometer z–axis resolution was used with a 50× objective to capture the 3D topography at three different areas of each sample. Three scanning areas were chosen to account for the potential variations of the patterns along the surface. The average height R_z and roughness R_a for each surface were extracted from LSCM images using the ISO 4287:1997 standard. Based on these measured properties, the average skewness and the average kurtosis were also calculated. **Fig. 3** shows the comparison between the optical image and the laser scanning 3D height map of a functionalized sample captured with LSCM. Another essential piece of information that needs to be extracted from the height-filtered images is the density distribution (*i.e.*, number of mounds per unit surface area) of the microstructures on each surface. To accomplish this, Fast Fourier

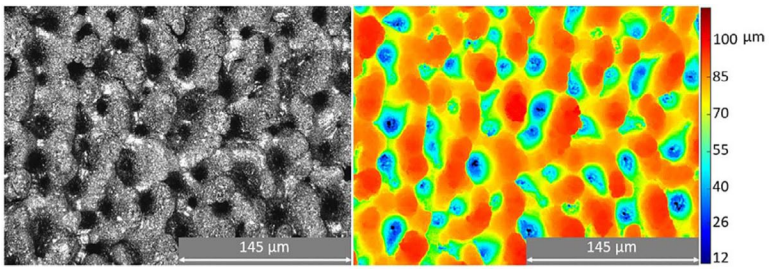

Fig. 3. (Left) 3D LSCM image of the FLSP aluminum sample captured at 50× magnification. (Right) 3D topographic map and height measurement of the same sample. This sample was produced with a pulse count of 490 and peak fluence of 2.01 J·cm^{-2} .

Transform (FFT) was implemented using MATLAB to find the strongest or the most frequent pattern in the LSCM images. Using this image processing technique, the dominant frequency in a 2D plane was found. However, in some images, a strong periodicity may be observed only in one direction. For such cases, the periodicity (or spacing) is usually assumed to be equal in both directions. The density distribution can then be determined by knowing the periodicity of the patterns and the scale of each LSCM image.

Now, to obtain the hemispherical emissivity of the samples in our study, first we measured the directional emissivity of the surfaces. To this aim, we utilized a FLIR A655sc thermal imaging camera with a spectral range of 7.5–14 µm to measure the surface temperature at different angles from 0° to 85° with increments of 5°. As a standard step in thermal imaging, a calibrated reference with a known emissivity is needed to accurately measure the emissivity of unknown specimens. In this work, black polyvinyl chloride electrical tape was used as the calibrated reference where its hemispherical, and directional emissivity were previously measured via Surface Optics SOC100 reflection-based instrument. We placed the tape next to a sample and heat them uniformly to 60 °C under the thermal camera. By adjusting the emissivity of the thermal camera to that of the calibrated reference, we can verify once the tape's temperature reaches 60 °C. Now, to extract the directional emissivity of the sample, first we can find the rate of incident energy on the thermal camera to be,

$$\begin{aligned} E_d &= A_s \cos\theta \Delta\Omega \int_{7.5\,\mu m}^{14\,\mu m} \left[\varepsilon_\lambda(\theta) I_{\lambda,b} + \rho_\lambda(\theta) I_{\lambda,bg}\right] d\lambda \\ &= A_s \cos\theta \Delta\Omega I_i(\theta) \end{aligned} \tag{3}$$

In the above equation, A_s is the sample's pixel surface area, $\Delta\Omega$ is the detection solid angle, θ is the polar angle of the camera's orientation, and $\varepsilon_\lambda(\theta)$ and $\rho_\lambda(\theta)$ are the spectral directional emissivity and reflectivity of the surface, respectively. As depicted, the radiation intensity incident on the camera consists of $\varepsilon_\lambda(\theta)I_{\lambda,b}$ which is due to the thermal emission from the surface, and $\rho_\lambda(\theta)I_{\lambda,bg}$ that represents the radiation from background reflected from the surface. By only considering the radiation inside the 7.5–14 μm window and assuming similar spectral distributions for $I_{\lambda,b}$ and $I_{\lambda,bg}$, we can simply replace the above integration with the total incident intensity, $I_i(\theta)$, which then yields,

$$\begin{aligned} I_i(\theta) &= \varepsilon(\theta)I_b + \rho(\theta)I_{bg} \\ &= \frac{\varepsilon(\theta)\sigma T_s^4}{\pi} + \frac{\rho(\theta)\sigma T_{bg}^4}{\pi} \end{aligned} \tag{4}$$

where T_s is the sample's surface temperature, T_{bg} is the background (room) temperature, and $\rho(\theta) = 1 - \varepsilon(\theta)$ based on Kirchhoff's law (*i.e.,* $\varepsilon_\lambda(\theta) = \alpha_\lambda(\theta)$) where the spectral dependence within 7.5–14 μm is inherently accounted for in the measurements from thermal camera. Now, by setting the emissivity of the thermal camera to one and focusing on the sample, a temperature T_d will be read by the camera which yields,

$$E_d = A_s \cos\theta \Delta\Omega \left(\frac{\sigma T_d^4}{\pi}\right)$$

By substituting $I_i(\theta)$ and E_d into Eq. (3) and some simplifications, we can obtain,

$$T_d^4 = \varepsilon(\theta)\, T_s^4 + \big(1 - \varepsilon(\theta)\big) T_{bg}^4 \tag{5}$$

where the only unknown is the directional emissivity of the sample, $\varepsilon(\theta)$. Further details of the emissivity measurement technique and verification can be found in Reference [27].

It is noteworthy that the spectral dependence is not considered when approximating the hemispherical emissivity, since the thermal imaging camera operates in the wavelength range of 7.5 to 14 μm. This, in effect, averages the measured emissivity with respect to the operating

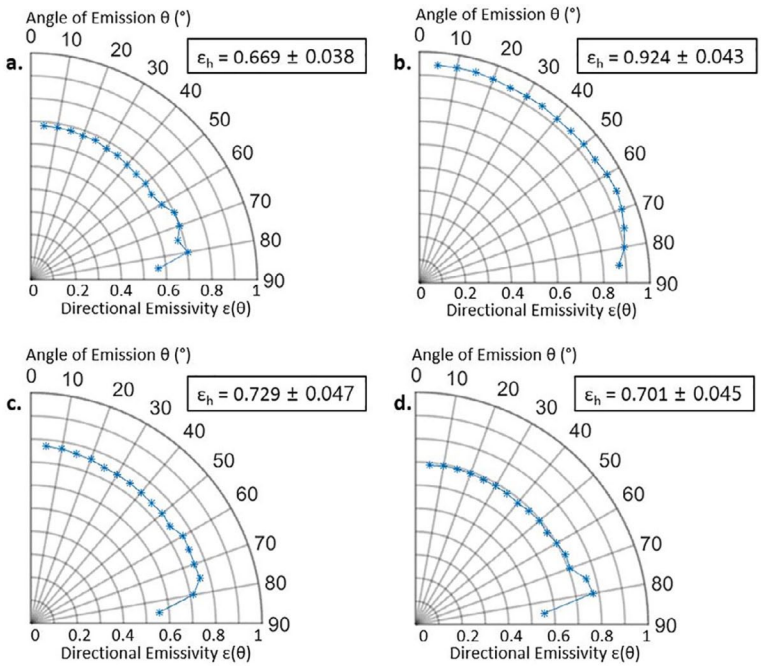

Fig. 4. Measured directional distribution of emissivity and hemispherical emissivity values for four different FLSP samples: (a) Pulse count of 490 and fluence of 2.0 J·cm^{-2}. (b) Pulse count of 6875 and fluence of 5.5 J·cm^{-2} . (c) Pulse count of 762 and fluence of 2.10 J·cm^{-2}. (d) Pulse count of 490 and fluence of 2.62 J ·cm^{-2} .

wavelength. Since the measured directional emissivities are for discrete angles, a numerical integration must be employed to calculate the hemispherical emissivity. For the approximation, the average between the rectangular and trapezoidal numerical integration was used. The difference between the approximate error of both methods yields the overall numerical uncertainty in calculating the hemispherical emissivity [27]. **Fig. 4** shows the measured directional and hemispherical emissivity of four different samples. The results depict that the magnitudes of the peak fluence and pulse count play decisive roles in the outcome of the overall emissivity. This is expected since the oxide layer thickness, structure height, and the periodicity of the microstructures depend on the magnitudes of the peak fluence and pulse count. A beam with lower fluence will result in finer structures, whereas a beam with higher fluence will result in coarser structures. In addition, at higher fluences the oxide layer is not uniform, resulting in a lower emissivity. Hence, there exists an optimal peak fluence and pulse count that will yield an optimal emissivity.

4. Data-driven prediction of hemispherical emissivity

In this study, 116 different samples were fabricated, characterized, and tested to build the study's dataset. The dataset consists of (*i*) laser operating parameters: pulse count P_c, fluence F_p, and total fluence F_t; (*ii*) surface characteristics data: average height R_z, average roughness R_a, average skewness S_k, average kurtosis K_u, mound surface area to planar area ratio S_A, and mound concentration (or density) D; and (*iii*) the measured hemispherical emissivity, ε_h. In addition, we collected 250 LSCM images from these samples. Multiple images were taken from different areas of each sample to create the image dataset.

In order to test the capabilities of AI for emissivity prediction, we studied two different scenarios. First, we wanted to know if AI can be employed to predict the (specific range of) emissivity of a new sample just based on its 3D LSCM image, without providing any other information about its surface characteristics or fabrication parameters. In other words, if we have a 3D surface morphology image of a sample without knowing anything else about it, can we estimate its expected emissivity within a narrow range? The successful accomplishment of this step is particularly advantageous for cases where an approximate surface radiative property is needed, and the only available data is a 3D morphology image of the sample and prior knowledge of the processing conditions. In the second scenario, we wanted to go one step further to know if we can precisely predict the actual emissivity of a new FLSP sample based on its surface characteristics data and laser operating parameters. Attaining such a model will provide us with a powerful tool that obviates the need for costly procedures to measure sample's surface radiative properties. Furthermore, such a model can enable reverse engineering of surfaces with desired emissivities to obtain the required processing parameters.

To test the feasibility of the first scenario, we used the measured hemispherical emissivity as the ground truth and divided the entire image dataset into seven categories ranging between 0.599 and 1, as illustrated in **Fig. 5.**

Throughout this study, we used a split validation method by randomly dividing the dataset into training, validation, and final test subsets with an 80:10:10 split ratio. We developed an AI model, *Model 1* , that solely used the LSCM images. As a precursor to this model, we

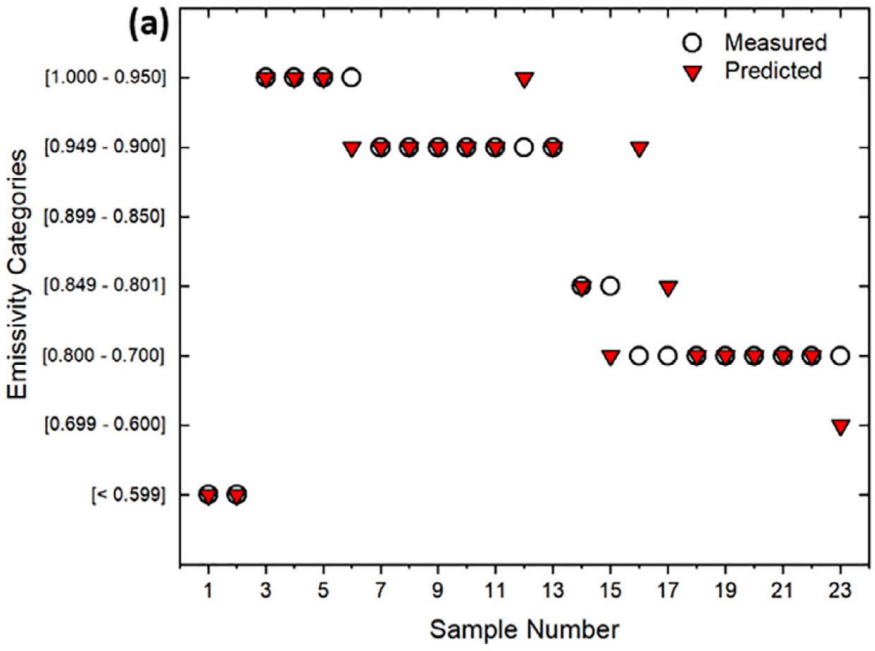

(b)

Predicted / Measured	1.000 – 0.950	0.949 – 0.900	0.899 – 0.850	0.849 – 0.801	0.800 – 0.700	0.699 – 0.600	<0.599	Class. Recall
1.000 – 0.950	3	1						75.0%
0.949 – 0.900	1	6						85.7%
0.899 – 0.850			0					0.0%
0.849 – 0.801				1	1			50.0%
0.800 – 0.700		1		1	5	1		62.5%
0.699 – 0.600						0		0.0%
<0.599							2	100.0%
Class. Precision	75.0%	75.0%	0.0%	50.0%	83.3%	0.0%	100.0%	

Fig. 5. (a) Classification results for *Model 1* , where the CNN's extracted features were used as inputs. Here, an error is predominantly present between categories close to each other, suggesting that some samples have similar surface features, thus confusing the CNN feature extractor. (b) Confusion matrix depicting the classification error in our *Model 1* . A green shaded area represents a positive (correct) response and a red shaded area represents a negative (incorrect) response. From the positive and negative responses, the classification precision (i.e., the ratio of correct predictions to the total relevant samples) and recall (i.e., the ratio of correct predictions to the total predicted cases) were calculated for each emissivity range. *Model 1* was tested on a total of 23 images.

implemented transfer learning (TL) by adopting VGG16 CNN architecture that was pre-trained on the ImageNet dataset. VGG16 is an established CNN architecture consisting of 16 computational layers. Visual Geometry Group (VGG) first introduced VGG16 in 2014 as a successful architecture classifying ImageNet dataset. This model uses large kernel-sized filters with multiple small kernel-sized filters resulting in 13 convolution layers with 3 fully connected layers. Training a CNN, such as VGG16 requires a large dataset and is computationally expensive. An alternative approach to mitigate these problems is TL. TL is a technique in which a model developed for one image analysis task is utilized as the basis for another model for a different image analysis task. Since a well-trained model is used as the starting point, the required processing and data reduces significantly for a TL model. More details regarding TL and the VGG16 CNN architecture can be found in [47]. To use this CNN as a feature extractor from the LSCM images, we replaced the final layer with 7 nodes to classify the images into the corresponding seven emissivity categories. A fine-tuning training approach was used by leaving the convolution layers of VGG16 unfrozen letting the weights to be updated during the training process. We initialized the classifier layers with random weights and trained the CNN using Adam optimizer with early stoppage criteria. We implemented the model using Tensor-flow (Keras) on a workstation comprised of an Intel(R) Xeon(R) Gold 6128 processor, 64GB of DDR4 RAM, and an NVIDIA Quadro P5000 graphic card.

Fig. 5 shows the results obtained from the developed *Model 1*. It can be seen from Fig. 5(a) that the model performed well and there is a great match for the majority of our test samples. It can be noted that there is a mismatch in the classification of samples 6, 12, 15, 16, 17, and 23. From the confusion matrix in Fig. 5(b), it can be observed that the error is predominantly present between adjacent categories, except for sample number 16. The mismatch can be attributed to the samples having similar surface features between the adjacent categories, thus confusing the CNN. It should be noted that by increasing the size and diversity of the image dataset, the model could get trained much better, significantly improving its classification ability and mitigating such confusion between neighboring categories. With a larger dataset, the width of the selected categories could also be narrower to improve the accuracy of the estimations.

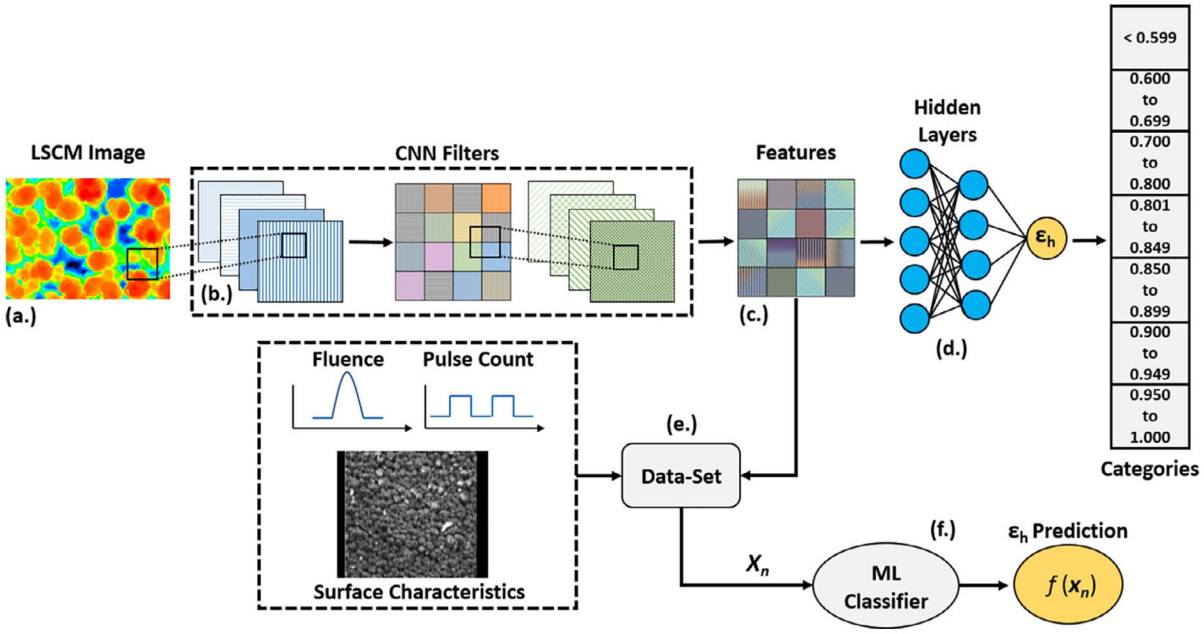

Fig. 6. General description of the AI architecture implemented in *Model 2* to predict the emissivity of the FLSP samples. **(a)** Here, each captured LSCM image serves as an input to our CNN architecture. **(b)** The initial LSCM images are processed one-by-one, through a series of convolutional filters that produce a feature vector. **(c)** Final feature vector then serves as an input into **(d)** *Model 1*, a general neural network that classifies each image into seven different emissivity categories. **(e)** A comprehensive dataset is built consisting of the laser operating parameters, measured surface characteristics and the detected features of the LSCM images. Then this data is fed into **(f)**, our *Model 2* that predicts the emissivity as a function of the input parameters.

Now, to demonstrate the application of AI in the second scenario, we developed *Model 2*. For this model, we combined the extracted features from the LSCM images with laser operating parameters and surface characteristics to build a comprehensive dataset. **Fig. 6** illustrates the AI architecture that was implemented by combining the image processing through deep-learning with several machine-learning classifiers to predict the emissivity. In this study, we refer to classifiers as the type of machine-learning models implemented to perform a regression analysis for prediction. These classifiers included *k*-nearest neighbor (kNN), artificial neural network (ANN), generalized linear model (GLM), W-M5P, and decision tree (DT). A detailed explanation of these classifiers can be found elsewhere and will not be repeated here [48–51]. We used the training subset (80% of our dataset) to develop this

Table 1 Prediction performance of different machine-learning classifiers in *Model 2.*

Model	*RMSE*	*ABS*	R^2
W-M5P	0.049	0.035 ± 0.034	0.966
GLM	0.066	0.055 ± 0.038	0.952
kNN	0.047	0.036 ± 0.030	0.978
DT	0.039	0.026 ± 0.029	0.979
ANN	0.039	0.030 ± 0.025	0.980

model. Hyperparameters were optimized iteratively on the validation subset using a grid search strategy. The final models were tested on the test subset that was isolated from the training and validation process. The performance of each model on the test subset is summarized and reported in **Table 1**, where root mean square error (*RMSE*), absolute error (*ABS*), and the coefficient of determination (R^2) are tabulated for comparison.

From Table 1, it can be observed that DT and ANN outperformed the rest of the classifiers. The obtained predictions from *Model 2* by using DT and ANN classifiers are illustrated with red markers in **Fig. 7**. It can be observed that both classifiers performed well with great match between the predictions and the measurements. For the sake of comparison, we have also included the prediction results using the same classifiers, but this time without the inputs from *Model 1* (*i.e.,* excluding the classifications obtained in *Model 1* from the inputs). Blue markers in Fig. 7 represent such predictions made based on the surface characteristics and the laser processing parameters. The comparison between the red and blue markers in Fig. 7(a) demonstrates that DT performed well with and without image-based classifications, showing approximate errors of 3.31% and 1.05%, respectively. However, the importance of inputting the image-based classifications on improving the predictions can be witnessed in Fig. 7(b) using the ANN classifier. It can be seen that the approximate error of ANN predictions significantly drops from 17.51% to 3.88% when considering the image-based classifications.

Now, to better understand the errors observed in some cases, we need to look into the individual data points. It can be seen that for samples number 6 and 12, there is a large deviation from the true value of measured emissivity in both DT and ANN methods when including the image-based classifications (i.e., red markers). This can be directly

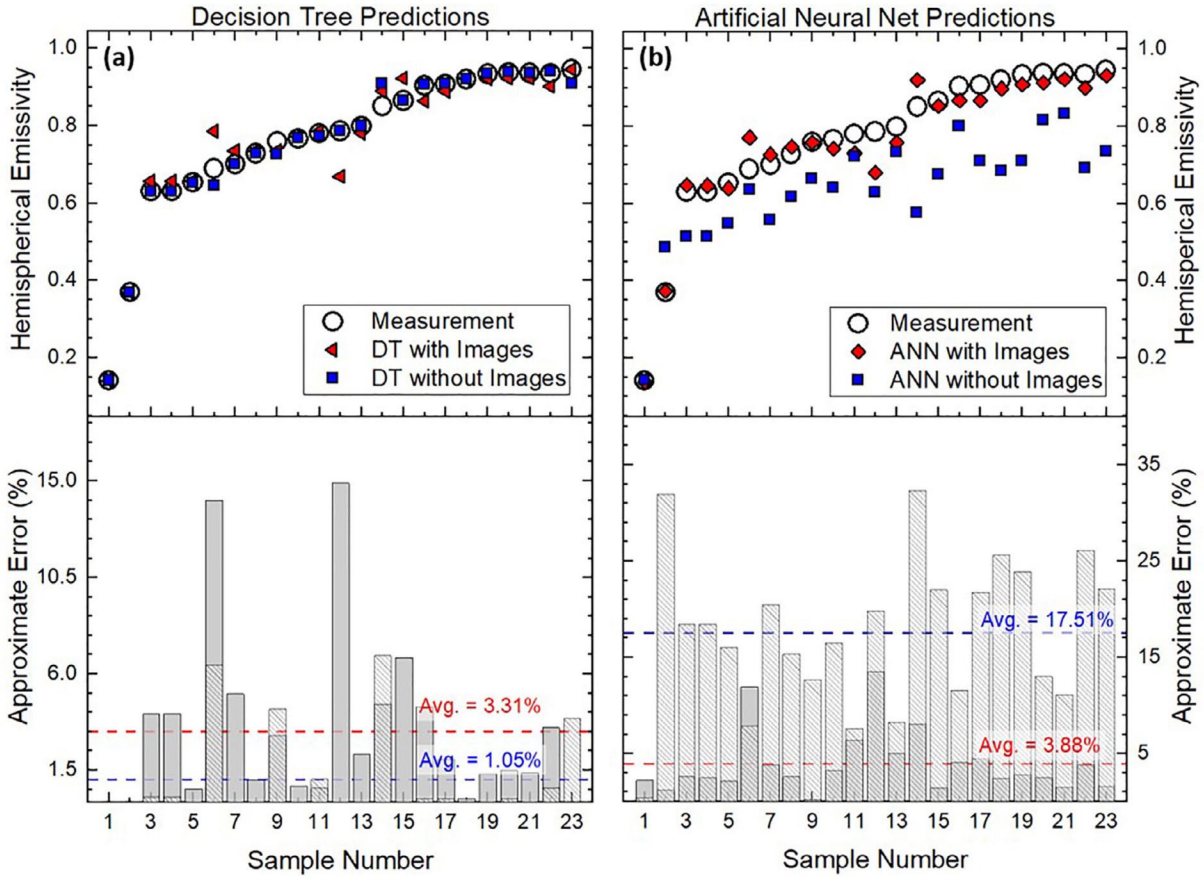

Fig. 7. Prediction results from *Model 2* using **(a)** decision tree (DT) classifier, and **(b)** artificial neural network (ANN) classifier. In both plots, the red markers represent the results obtained by including the images input (i.e., classifications from *Model 1*) and blue markers represent the results without images input. The approximate prediction errors are also shown for both cases in each classifier. It should be noted that these results are obtained from the testing subset (i.e., 10% of our dataset) which has been isolated from the training and validation subsets.

attributed to the error that originated in feature extraction from the CNN in *Model 1* (see Fig. 5) that has now propagated into *Model 2*. This type of error can be addressed by acquiring a larger LSCM image-set and hence better performance of the CNN. Thus, the slight increase in the approximate error of DT when including the image-based classifications is because of the high mismatch from *Model 1* at samples number 6 and 12. Another important factor that can limit the accuracy of predictions and must be considered is the distribution of available samples within the

training subset. To elucidate this, we can observe that Fig. 7(b) shows a relatively high error in samples number 2 and 14 when the image-based classifications are not considered (i.e., blue markers). The high approximate error of ANN in these two cases can be attributed to the fact that samples 2 and 14 correspond to the specific ranges of emissivity where we had limited available data. In other words, the number of samples that fit into those two categories was limited compared to the other categories. This can potentially lead to inadequate training of ANN on specific emissivity ranges short on samples. Hence, this demonstrates the advantage of combining image-based classifications with surface characteristics and fabrication inputs into our *Model 2* , when a limited dataset is available for training.

5. Conclusion

In this study, we have demonstrated the advantage of applying AI techniques for emissivity prediction of complex surfaces. For this purpose, we fabricated 116 aluminum samples using FLSP. A comprehensive dataset consisting of surface characteristics, fabrication parameters, and 250 LSCM images from these surfaces was established. The directional emissivity of each sample was measured using a thermal imaging camera within 7.5 to 14 μm, and was used to calculate the hemispherical emissivity.

We investigated the application of AI for emissivity prediction in two different cases. In case 1, we could show that the specific range of emissivity for a given surface could be approximated merely based on its 3D morphology image. We pre-trained a CNN that served as a feature extractor on our training image dataset and developed an ANN to classify the test samples into seven emissivity categories. The obtained results revealed the great advantage of AI-based methods in estimating the emissivity by image processing. For case 2, we demonstrated that the combination of deep-learning and machine-learning techniques could be implemented to accurately predict the emissivity of FLSP samples based on their surface characteristics and fabrication parameters. To accomplish this, several machine-learning classifiers were applied to the dataset where DT and ANN outperformed other classifiers with approximate errors of 3.31% and 3.88%, respectively.

The promising performance of these data-driven models can open new paradigms for predicting physical phenomena that might otherwise be difficult to predict by classical physics-based modeling or may require tedious experimental procedures. However, it is noteworthy that as a standard limitation of AI, the obtained data-driven models are always restricted to the boundaries of the training domain, meaning that their application beyond the training dataset will be unreliable. Similarly, to obtain a data-driven predictive model for any other material, the AI model would need to be retrained on the proper dataset.

• • • • • •

Competing Interests The authors declare there are no known competing financial interests or personal relationships that could appear to influence the work reported in this paper.

CRediT authorship contributions

Greg Acosta: Methodology, Software, Validation, Formal analysis, Investigation, Writing–original draft, Visualization.

Andrew Reicks: Validation, Formal analysis, Investigation, Writing–original draft, Visualization.

Miguel Moreno: Formal analysis, Investigation.

Alireza Borjali: Conceptualization, Methodology, Software, Validation, Formal analysis, Writing–original draft.

Craig Zuhlke: Conceptualization, Investigation, Resources, Supervision.

Mohammad Ghashami: Conceptualization, Methodology, Resources, Supervision, Project administration.

Acknowledgments This work was supported in part by the National Aeronautics and Space Administration (NASA) Nebraska Space Grant NNX15AI09H. The research was performed in part in the Nebraska Nanoscale Facility: National Nanotechnology Coordinated Infrastructure and the Nebraska Center for Materials and Nanoscience (and/or NERCF), which are supported by the National Science Foundation under Award ECCS: 2025298 , and the Nebraska Research Initiative. We would also like to acknowledge the NASA Nebraska Space Grant Fellowship 4403071026358 and the NASA-EPSCoR Mini-Grant 4403071025314 for their financial support.

References

[1] Zhang G, Xue Y, Liu P, Guo A, Du H, Yan L, Liu J. High emissivity double-layer coating on the flexible aluminum silicate fiber fabric with enhanced interfacial bonding strength and high temperature resistance. J Eur Ceram Soc 2021;41(2):1452–8.

[2] Bird RK, Wallace TA, Sankaran SN. Development of protective coatings for high-temperature metallic materials. J Spacecr Rockets 2004;41(2):213–20.

[3] Pidan S, Auweter-Kurtz M, Herdrich G, Fertig M. Recombination coefficients and spectral emissivity of silicon carbide-based thermal protection materials. J Thermophys Heat Transf 2005;19(4):566–71.

[4] Li N, Wang J, Liu D, Huang X, Xu Z, Zhang C, Zhang Z, Zhong M. Selective spectral optical properties and structure of aluminum phosphate for daytime passive radiative cooling application. Sol Energy Mater Sol Cells 2019;194:103–10.

[5] Raman AP, Abou Anoma M, Zhu L, Rephaeli E, Fan S. Passive radiative cooling below ambient air temperature under direct sunlight. Nature 2014;515(7528):540–4.

[6] Kim Y, Kim M-J, Kim Y-S, Lee H, Lee S-M. Nanostructured radiation emitters: design rules for high-performance thermophotovoltaic systems. ACS Photonics 2019;6(9):2260–7.

[7] Burger T, Sempere C, Roy-Layinde B, Lenert A. Present efficiencies and future opportunities in thermophotovoltaics. Joule 2020.

[8] Krishna A, Lee J. Morphology-driven emissivity of microscale treelike structures for radiative thermal management. Nanoscale Microscale Thermophys Eng 2018;22(2):124–36.

[9] Krishna A, Kim JM, Leem J, Wang MC, Nam S, Lee J. Ultraviolet to mid-infrared emissivity control by mechanically reconfigurable graphene. Nano Lett 2019;19(8):5086–92.

[10] He X, Li Y, Wang L, Sun Y, Zhang S. High emissivity coatings for high temperature application: progress and prospect. Thin Solid Films 2009;517(17):5120–9.

[11] Cockeram B, Measures D, Mueller A. The development and testing of emissivity enhancement coatings for thermophotovoltaic (TPV) radiator applications. Thin Solid Films 1999;355:17–25.

[12] Lempereur C, Andral R, Prudhomme J. Surface temperature measurement on engine components by means of irreversible thermal coatings. Meas Sci Technol 2008;19(10):105501.

[13] Manara J, Zipf M, Stark T, Arduini M, Ebert H-P, Tutschke A, Hallam A, Hanspal J, Langley M, Hodge D, et al. Long wavelength infrared radiation thermometry for non-contact temperature measurements in gas turbines. Infrared Phys Technol 2017;80:120–30.

[14] Simpson A, Fitton R, Rattigan I, Marshall A, Parr G, Swan W. Thermal performance of thermal paint and surface coatings in buildings in heating dominated climates. Energy Build 2019;197:196–213.

[15] Fantucci S, Serra V. Investigating the performance of reflective insulation and low emissivity paints for the energy retrofit of roof attics. Energy Build 2019;182:300–10. 7

[16] Manickavasagan A, Jayas D, White N, Jian F. Thermal imaging of a stored grain silo to detect a hot spot. Appl Eng Agric 2006;22(6):891–7.

[17] Brandt R, Bird C, Neuer G. Emissivity reference paints for high temperature applications. Measurement 2008;41(7):731–6.

[18] Liu X, Tyler T, Starr T, Starr AF, Jokerst NM, Padilla WJ. Taming the blackbody with infrared metamaterials as selective thermal emitters. Phys Rev Lett 2011;107(4):045901.

[19] Liu X, Padilla WJ. Thermochromic infrared metamaterials. Adv Mater 2016;28(5):871–5.

[20] Li J, Wuenschell J, Li Z, Bera S, Liu K, Tang R, Du H, Ohodnicki PR, Shen S. Fiber coupled near-field thermoplasmonic emission from gold nanorods at 1100 k. Small 2021;17(17):2007274.

[21] Baranov DG, Xiao Y, Nechepurenko IA, Krasnok A, Alu‘ A, Kats MA. Nanophotonic engineering of far-field thermal emitters. Nat Mater 2019;18(9):920–30.

[22] Hu R, Xi W, Liu Y, Tang K, Song J, Luo X, Wu J, Qiu C-W. Thermal camouflaging metamaterials. Mater Today 2021.

[23] Florian C, Kirner SV, Krüger J, Bonse J. Surface functionalization by laser-induced periodic surface structures. J Laser Appl 2020;32(2):022063.

[24] Fan P, Zhong M, Li L, Huang T, Zhang H. Rapid fabrication of surface micro/ nano structures with enhanced broadband absorption on cu by picosecond laser. Opt Express 2013;21(10):11628–37.

[25] Chen T, Wang W, Tao T, Pan A, Mei X. Multi-scale micro-nano structures prepared by laser cleaning assisted laser ablation for broadband ultralow reflectivity silicon surfaces in ambient air. Appl Surf Sci 2020;509:145182.

[26] Tang G, Hourd AC, Abdolvand A. Nanosecond pulsed laser blackening of copper. Appl Phys Lett 2012;101(23):231902.

[27] Reicks A, Tsubaki A, Anderson M, Wieseler J, Khorashad LK, Shield JE, Gogos G, Alexander D, Argyropoulos C, Zuhlke C. Near-unity broadband omnidirectional emissivity via femtosecond laser surface processing. Commun Mater 2021;36(2):1–11.

[28] Sizemore NE, Nogueira ML, Greis NP, Davies MA. Application of machine learning to the prediction of surface roughness in diamond machining. Procedia Manuf 2020;48:1029–40.

[29] Wuest T, Weimer D, Irgens C, Thoben K. Machine learning in manufacturing: advantages, challenges, and applications. Prod Manuf Res 2016;4(1):23–45.

[30] Kim D-H, Kim TJ, Wang X, Kim M, Quan Y-J, Oh JW, Min S-H, Kim H, Bhandari B, Yang I, et al. Smart machining process using machine learning: A review and perspective on machining industry. Int J Precis Eng Manuf Green Technol 2018;5(4):555–68.

[31] Jurkovic Z, Cukor G, Brezocnik M, Brajkovic T. A comparison of machine learning methods for cutting parameters prediction in high speed turning process. J Intell Manuf 2018;29(8):1683–93.

[32] Kang HH, Kaya M, Hajimirza S. A data driven artificial neural network model for predicting radiative properties of metallic packed beds. J Quant Spectrosc Radiat Transfer 2019;226:66–72.

[33] Mishra S, Molinaro R. Physics informed neural networks for simulating radiative transfer. J Quant Spectrosc Radiat Transf 2021;270:107705.

[34] Raissi M, Perdikaris P, Karniadakis GE. Physics-informed neural networks: A deep learning framework for solving forward and inverse problems involving nonlinear partial differential equations. J Comput Phys 2019;378:686–707.

[35] Borjali A, Monson K, Raeymaekers B. Predicting the polyethylene wear rate in pin-on-disc experiments in the context of prosthetic hip implants: Deriving a data-driven model using machine learning methods. Tribol Int 2019;133(January): 101–10.

[36] Xiong J, Shi S-Q, Zhang T-Y. A machine-learning approach to predicting and understanding the properties of amorphous metallic alloys. Mater Des 2020;187:108378.

[37] Akhil V, Raghav G, Arunachalam N, Srinivas D. Image data-based surface texture characterization and prediction using machine learning approaches for additive manufacturing. J Comput Inf Sci Eng 2020;20(2):021010.

[38] So S, Badloe T, Noh J, Bravo-Abad J, Rho J. Deep learning enabled inverse design in nanophotonics. Nanophotonics 2020;9(5):1041–57.

[39] Peurifoy J, Shen Y, Jing L, Yang Y, Cano-Renteria F, DeLacy BG, Joannopoulos JD, Tegmark M, Soljačić M. Nanophotonic particle simulation and inverse design using artificial neural networks. Sci Adv 2018;4(6):eaar4206.

[40] So S, Mun J, Rho J. Simultaneous inverse design of materials and structures via deep learning: demonstration of dipole resonance engineering using core–shell nanoparticles. ACS Appl Mater Interfaces 2019;11(27):24264–8.

[41] Liu Z, Zhu D, Rodrigues SP, Lee K-T, Cai W. Generative model for the inverse design of metasurfaces. Nano Lett 2018;18(10):6570–6.

[42] García-Esteban JJ, Bravo-Abad J, Cuevas JC. Deep learning for the modeling and inverse design of radiative heat transfer. Phys Rev Appl 2021;16(6):064006.

[43] Singh N, Alexander DR, Schiffern J, Doerr D. Femtosecond laser production of metal surfaces having unique surface structures that are broadband absorbers. J Laser Appl 2006;18(3):242–4.

[44] Ou Z, Huang M, Zhao F. The fluence threshold of femtosecond laser blackening of metals: the effect of laser-induced ripples. Opt Laser Technol 2016;79:79–87.

[45] Le Harzic R, Huot N, Audouard E, Jonin C, Laporte P, Valette S, Fraczkiewicz A, Fortunier R. Comparison of heat-affected zones due to nanosecond and femtosecond laser pulses using transmission electronic microscopy. Appl Phys Lett 2002;80(21):3886–8.

[46] Huang H, Yang L-M, Bai S, Liu J. Blackening of metals using femtosecond fiber laser. Appl Opt 2015;54(2):324–33.

[47] Morid MA, Borjali A, Del Fiol G. A scoping review of transfer learning research on medical image analysis using ImageNet. Comput Biol Med 2021;128:104115.

[48] Hastie T, Tibshirani R. Discriminant adaptive nearest neighbor classification. IEEE Trans Pattern Anal Mach Intell 1996;18(6):607–16.

[49] Dreiseitl S, Ohno-Machado L. Logistic regression and artificial neural network classification models: a methodology review. J Biomed Inform 2002;35(5-6):352–9.

[50] Kiliç S. Linear regression analysis. Psychiatry Behav Sci 2013;3(2):90.

[51] Rokach L, Maimon OZ. Data Mining with Decision Trees: Theory and Applications, Vol. 69. World scientific; 2007.